MNRAS **000**, 1–4 (2015) Preprint 17 November 2015 Compiled using MNRAS LATEX style file v3.0

An Efficient E-field Parallel Imaging Calibration Algorithm for Next-Generation Radio Telescopes

Adam P. Beardsley,[1★] Nithyanandan Thyagarajan,[1] Judd D. Bowman[1] and Miguel F. Morales[2]
[1]*Arizona State University, School of Earth and Space Exploration, Tempe, AZ 85287, USA*
[2]*University of Washington, Department of Physics, Seattle, WA 98195, USA*

Accepted XXX. Received YYY; in original form ZZZ

ABSTRACT
Abstract here (250 words)

Key words: instrumentation: interferometers – techniques: image processing – techniques: interferometric

1 INTRODUCTION

In order to satisfy the survey speeds required for precision cosmology as well as searches for fast radio transients, radio astronomy is undergoing a paradigm shift toward interferometers consisting of hundreds to thousands of small, widefield antennas. Many arrays with this design are already built or under construction including the Hydrogen Epoch of Reionization Array[1] (HERA), the Murchison Widefield Array (MWA;Tingay et al. 2013; Bowman et al. 2013), the Precision Array for Probing the Epoch of Reionization (PAPER; Parsons et al. 2010), the LOw Frequency ARray (LOFAR;van Haarlem et al. 2013), the Canadian Hydrogen Intensity Mapping Experiment (CHIME,Bandura et al. 2014), the Long Wavelength Array (LWA, Ellingson et al. 2013), and the low frequency Square Kilometer Array (SKA1-Low Mellema et al. 2013).

Traditional radio correlators cross-multiply the voltage signals from all pairs of antennas, and the computation scales as the number of antennas squared, $O(N_{\rm ant}^2)$ (Bunton 2004). As the number of elements in future arrays grows, the computational cost will become prohibitively expensive, and exploring efficient correlator schemes is essential to enable next generation instruments (Lonsdale et al. 2000). Meanwhile, radio transient monitoring requires access to high time and frequency resolution data. For example, Fast Radio Bursts (FRBs) are highly unexplored at low frequencies (< 1 GHz), but are expected to occur on timescales $\Delta t \sim$ 1–10 ms (Thornton et al. 2013). Recording the full visibility matrix for $N_{\rm ant} \gtrsim 10^3$ arrays at this timescale leads to extremely high data write rates.

Direct imaging correlators are a new variety of radio correlator which aim to alleviate both the computational strain of forming $N_{\rm ant}^2$ correlations and the high data throughput associated with short timescale science. This is done by performing a spatial fast Fourier transform (FFT) to image the antenna voltages, then squaring and averaging in time. This process scales as $O(N_{\rm g} \log_2 N_{\rm g})$, where $N_{\rm g}$ is the number of grid points in the FFT (Morales 2011; Tegmark & Zaldarriaga 2009; Tegmark & Zaldarriaga 2010). For certain classes of telescopes, significantly those envisioned for next generation cosmology experiments, this scaling is a large improvement over the $N_{\rm ant}^2$ scaling of traditional methods. Furthermore, because images are generated online, the native output bandwidth will be lowered (assuming $N_{\rm g} < N_{\rm ant}^2$), and has the potential to be lowered even further with online transient processing.

A handful of prototype direct imaging correlators have been tested on arrays including the Basic Element for SKA Training II (BEST-2) array (Foster et al. 2014), the Omniscope (Zheng et al. 2014), and an earlier pulsar timing experiment at GHz frequencies (Otobe et al. 1994; Daishido et al. 2000). Each of these are examples of so-called FFT correlators – a subclass of direct imaging correlators which rely on identical antennas with restricted placement, which allows the FFT to be performed without gridding. We recently released the E-field Parallel Imaging Correlator (EPIC; Thyagarajan et al. 2015), which is a software implementation of the Modular Optimal Frequency Fourier (MOFF; Morales 2011) imaging algorithm. This architecture leverages the software holography/A-transpose framework to grid electric field data streams before performing the spatial FFT, allowing for an optimal map without placing constraints on array layout or requiring identical antennas (Morales & Matejek 2009; Bhatnagar, S. et al. 2008; Tegmark 1997).

A challenge common to all direct imaging algorithms is calibration of the antenna gains. Traditionally, pair-wise visibilities are written to disk and used to calibrate offline. However, a direct imaging correlator mixes the signals from all antennas before averaging and writing to disk, making calibration a requirement at the front end. Previous solutions have involved applying calibration solutions generated from a parallel FX correlator (Zheng et al. 2014; Foster et al. 2014), or integrating a dedicated FX correlator which periodically formed the full visibility matrix to solve for gains (Wijnholds & van der Veen 2009; de Vos et al. 2009). While these solutions were sufficient to enable the exploration of FFT correlators and beamformers, they will not scale to future arrays with $N_{\rm ant} \gtrsim 10^3$.

★ E-mail: Adam.Beardsley@asu.edu
[1] http://reionization.org

© 2015 The Authors

Here we present the E-field Parallel Imaging Calibration (EPICal) algorithm – a novel solution to the calibration problem, which can be integrated into direct imaging correlators and scales only as the number of antennas, $O(N_{\rm ant})$. This method uses a correlation of the uncalibrated antenna signal stream with an output image pixel from the backend of the correlator to solve for the complex gains of the antennas. In the limit of a simple sky, the algorithm reduces to the self-cal algorithm, and even in a complex limit can be shown to be equivalent to visibility-based solutions. An example implementation of the algorithm is available with the EPIC software package[2] We establish the mathematical framework and derive the calibration algorithm in §2. We then demonstrate the algorithm in simulations in §3, and apply to a sample LWA data set in §4. Then we discuss the noise properties of the resulting gain solutions in §5. Finally we conclude and discuss potential extensions to the algorithm in §6.

2 MATHEMATICAL FRAMEWORK

We begin by establishing the mathematical framework for the calibration problem. We derive the calibration solutions for the MOFF algorithm (adopting the notation of Thyagarajan et al. 2015), but note the result is easily extended to FFT correlator algorithms by removing the gridding step.

The electric field incident on the ground, $\widetilde{E}(\mathbf{r}, f, t)$, is related to the sky electric field, $E(\hat{\mathbf{s}}, f, t)$, through a Fourier transform.

$$\widetilde{E}(\mathbf{r}, f, t) = \int E(\hat{\mathbf{s}}, f, t) e^{-2\pi i \mathbf{r}\cdot\hat{\mathbf{s}}}\, \mathrm{d}^2\hat{\mathbf{s}} \tag{1}$$

Here $\hat{\mathbf{s}}$ denotes the sine-projected unit vector for the sky angle, $\mathbf{r}$ is the observer's location (measured in wavelengths relative to an arbitrary origin), and f and t denote the frequency and time dependence, respectively. We will encounter several quantities which we attempt to estimate. We distinguish the "true" values with a superscript T, while the estimates are denoted with a hat. We define the true antenna signal as a convolution of the antenna voltage pattern, $\widetilde{W}$, with the electric field on the ground.

$$\widetilde{E}_a^T(f, t) \equiv \int \widetilde{W}_a(\mathbf{r} - \mathbf{r}_a)\widetilde{E}(\mathbf{r}, f, t)\, \mathrm{d}^2\mathbf{r} \tag{2}$$

The subscript a labels the antenna, and $\mathbf{r}_a$ is the location of antenna a.

We next model the measured, uncalibrated electric field as a multiplicative complex gain and an additive noise term applied to the true antenna electric field.

$$\widetilde{E}_a(f, t) = g_a^T(f, t)\widetilde{E}_a^T(f, t) + \widetilde{n}_a(f, t) \tag{3}$$

Note that this quantity is neither a true or estimated value. The noise term is strictly receiver noise – noise introduced by the instrument. Any sky noise is implicitly included in the time dependence of the sky electric field. As the noise of modern low frequency arrays is heavily dominated by sky noise, we will neglect $\widetilde{n}_a$ for now, but will inspect its effects at the end of this section.

The goal of our calibration algorithm will be to estimate the antenna gains. We will assume the gains have no time dependence within the timescale of finding our solutions. cite someone about gain stability. Furthermore, we will treat each frequency channel independently, and drop the f to simplify notation.

The MOFF algorithm next calls for a calibration. For now we will assume we have formed an estimate of the gains after n iterations of a calibration loop, and can apply these gains. Typically calibration amounts to dividing the measured fields by the complex gain, or multiplying by the complex conjugate of the gain. We will abstain from this choice for now, and instead use a multiplicative factor $h_a^{(n)}$ to represent the application of our $n^{\rm th}$-loop estimate of the gain for antenna a.

$$\hat{\widetilde{E}}_a = h_a^{(n)}\widetilde{E}_a \tag{4}$$

A dirty image is next formed by gridding the calibrated fields with the antenna voltage pattern, Fourier transforming, squaring, and averaging in time. The estimated value for a pixel, $\hat{\mathbf{s}}_{\rm pix}$, can be expressed as

$$\hat{I}(\hat{\mathbf{s}}_{\rm pix}) = \left\langle \left| \frac{1}{N_{\rm ant}} \sum_i e^{2\pi i \mathbf{r}\cdot\hat{\mathbf{s}}_{\rm pix}} \sum_a \widetilde{W}_a(\mathbf{r}_i - \mathbf{r}_a) h_a^{(n)} g_a^T \widetilde{E}_a^T(t) \right|^2 \right\rangle_t . \tag{5}$$

This is the final output of the MOFF correlator. However, for calibration purposes we will be interested in the electric field image just prior to squaring and averaging.

$$\hat{E}(\hat{\mathbf{s}}_{\rm pix}, t) = \frac{1}{N_{\rm ant}} \sum_i e^{2\pi i \mathbf{r}_i\cdot\hat{\mathbf{s}}_{\rm pix}} \sum_a \widetilde{W}_a(\mathbf{r}_i - \mathbf{r}_a) h_a^{(n)} g_a^T \widetilde{E}_a^T(t) \tag{6}$$

We can simplify this expression by exchanging the sums to transform the beam term into sky coordinates.

$$\begin{aligned}\hat{E}(\hat{\mathbf{s}}_{\rm pix}, t) &= \frac{1}{N_{\rm ant}} \sum_a h_a^{(n)} g_a^T \widetilde{E}_a^T e^{2\pi i \hat{\mathbf{s}}_{\rm pix}\cdot\mathbf{r}_a} \sum_i \widetilde{W}_b(\mathbf{r}_i - \mathbf{r}_a) e^{2\pi i \hat{\mathbf{s}}_{\rm pix}\cdot(\mathbf{r}_i - \mathbf{r}_a)} \\ &= \frac{1}{N_{\rm ant}} \sum_a h_a^{(n)} g_a^T \widetilde{E}_a^T e^{2\pi i \hat{\mathbf{s}}_{\rm pix}\cdot\mathbf{r}_a} W_a(\hat{\mathbf{s}}_{\rm pix})\end{aligned} \tag{7}$$

Next we move toward the feedback calibration outlined in Morales 2011. The calibration loop described there assumed a simple sky of a single point source, but we aim for a more generalized solution for arbitrarily complex sky models. As such the quantity we wish to inspect is a correlation of the uncalibrated antenna signals input to the correlator with the holographic electric field image output from the correlator. We define the quantity,

$$C_{a,\hat{\mathbf{s}}_{\rm pix}}^{(n)} \equiv \left\langle \widetilde{E}_a(t)\hat{E}^*(\hat{\mathbf{s}}_{\rm pix}, t) \right\rangle_t , \tag{8}$$

where the superscript n again represents the quantity formed in the $n^{\rm th}$ calibration loop. Naturally, because the right hand side contains the output of the correlator, this will be an iterative process. The following will hold for any chosen pixel, $\hat{\mathbf{s}}_{\rm pix}$, though we will see it is advantageous to choose a pixel which contains a bright source.

Plugging equation 7 into equation 8, we find,

$$\begin{aligned}C_{a,\hat{\mathbf{s}}_{\rm pix}}^{(n)} &= \left\langle g_a^T \widetilde{E}_a^T(t) \frac{1}{N_{\rm ant}} \sum_b h_b^{*(n)} g_b^{T*} \widetilde{E}_b^{T*}(t) e^{-2\pi i \hat{\mathbf{s}}_{\rm pix}\cdot\mathbf{r}_b} W_b^*(\hat{\mathbf{s}}_{\rm pix}) \right\rangle_t \\ &= \frac{g_a^T}{N_{\rm ant}} \sum_b h_b^{*(n)} g_b^{T*} W_b^*(\hat{\mathbf{s}}_{\rm pix}) e^{-2\pi i \hat{\mathbf{s}}_{\rm pix}\cdot\mathbf{r}_b} \left\langle \widetilde{E}_a^T \widetilde{E}_b^{*T} \right\rangle_t \\ &= \frac{g_a^T}{N_{\rm ant}} \sum_b h_b^{*(n)} g_b^{T*} W_b^*(\hat{\mathbf{s}}_{\rm pix}) e^{-2\pi i \hat{\mathbf{s}}_{\rm pix}\cdot\mathbf{r}_b} \widetilde{V}_{ab}^T\end{aligned} \tag{9}$$

where in the second step we group time-dependent terms, and in the third we define the true visibilities as the correlation between true antenna electric field measurements. It is easy to see from here that the net effect of including the receiver noise term, $\widetilde{n}$

Finally, we estimate our solution by assuming our current estimate of the gains, $\hat{g}_b^{(n)}$ is approximately correct and substitute into

[2] http://github.com/nithyanandan/EPIC

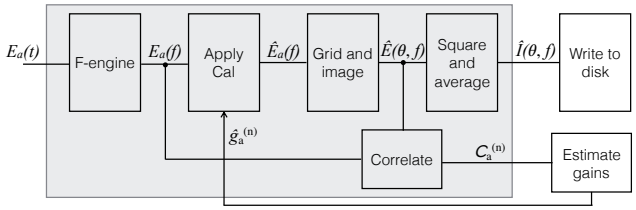

Figure 1. Caption goes here

the sum for the true gains. We also require model visibilities formed from sky and primary beam models in place of true visibilities.

$$\hat{g}_a^{(n+1)} = C_{a,\hat{\mathbf{s}}_{\rm pix}}^{(n)} N_{\rm ant} \left[\sum_b h_b^{*(n)} \hat{g}_b^{*(n)} W_b^*(\hat{\mathbf{s}}_{\rm pix}) e^{-2\pi i \hat{\mathbf{s}}_{\rm pix}\cdot\mathbf{r}_b} \widetilde{V}_{ab}^T \right]^{-1} \tag{10}$$

This equation is our prescription for estimating the antenna gains of a direct imaging array. The approach is iterative in nature, and requires a sky model. However, the sky model can be precomputed offline, and the online computation complexity scales only as $O(N_{\rm ant})$ as we form a $C_{a,\hat{\mathbf{s}}_{\rm pix}}^{(n)}$ for each antenna. In the case where $h_b = 1/g_b$, this simplifies slightly.

$$\hat{g}_a^{(n+1)} = C_{a,\hat{\mathbf{s}}_{\rm pix}}^{(n)} N_{\rm ant} \left[\sum_b W_b^*(\hat{\mathbf{s}}_{\rm pix}) e^{-2\pi i \hat{\mathbf{s}}_{\rm pix}\cdot\mathbf{r}_b} \widetilde{V}_{ab}^T \right]^{-1} \tag{11}$$

We note an encouraging analogy to the solutions found in Mitchell et al. 2008 (their equation 11). In the case where $\hat{\mathbf{s}}_{\rm pix}$ is the central pixel of the image, we see $C_{a,\hat{\mathbf{s}}_{\rm pix}}^{(n)}$ is simply the sum of visibilities involving antenna a in equation 9. This is equivalent to the numerator equation 11 in Mitchell et al. 2008, in the single polarization case. The denominator then is the sum over modeled visibilities, as in our equation 10 (save bookkeeping to track Fourier transform conventions and gain applications). The major difference in our solution is the inclusion of auto-correlations in both sums. If desired, a deployed system could adapt equation 10 to remove the auto-correlations. This would require generating these correlations, which again only scale as $O(N_{\rm ant})$, and are generally useful for array diagnostics.

We thus confirm what was shown for the simple-sky case in Morales 2011 – our calibration solutions are equivalent to those derived from visibility data. We will pursue this further in section 5.

We show schematically the process of calibrating a direct imaging correlator in figure 1. Computationally expensive steps that must be performed "on-chip" are shown inside the gray box. The uncalibrated antenna signals are tapped out after the F-engine and correlated against the output image pixel of interest. The correlated values are then passed off-chip to estimate the gains using equation 10, and additional fitting if desired. The gains are then passed back to the correlator to update the calibration for subsequent data streams.

3 SIMULATION

We first demonstrate our calibration method through a controlled simulation. The simulation software used is included in the EPIC package, and we follow a procedure based on that described in Thyagarajan et al. 2015, using the same toy-model sky with 10 point sources of flux density 10 Jy at random location. We assume perfect knowledge of the sky to build our model visibilities.

We use 64 frequency channels each 40 kHz, and each time-series is 25 μs long. However, because each channel is independent in the calibration loop we only show the central channel here. Using the MWA array layout (Beardsley et al. 2012), we select the inner 51 antennas within a square bounding box of 150 m. The antenna voltage pattern used is a 4.4 m square tophat on the ground.

In order to show our ability to recover unknown complex antenna gains, we create a set of random numbers with amplitude 1 ± 0.25, and completely random phase. These are our "true gains", and we apply them to the frequency-domain simulated antenna electric fields as in equation 3. Our analysis is blind to these values until the end of the process to check accuracy. We start with an initial guess of unity gains.

We next process 50 time stamps, creating both a short-term integrated image and $C_{a,\hat{\mathbf{s}}_{\rm pix}}^{(0)}$ correlations. Unless otherwise specified, the software automatically selects the brightest source in the sky model to choose the correlation pixel. We use our correlation values to update the gains. We found that simply using equation 10 resulted in large oscillations in the solutions, which eventually converged. To mitigate this we introduce a tunable damping factor, $0 < \Delta \leq 1$, which is used to attenuate the gain update, effectively giving the solutions memory of previous iterations. Through experimentation we found $\Delta = 0.65$ resulted in the quickest convergence for this simulation.

We continue the calibration loop by updating our gain estimates, dividing the data by the gains, forming images and $C_{a,\hat{\mathbf{s}}_{\rm pix}}^{(n)}$ correlations to form the next estimate. This process was repeated 20 times.

4 APPLICATION TO LWA DATA

Reference for Cyg-A: Cohen et al. 2007. Ref for Cas-A: Kassim et al. 2007. Apply to LWA data.

5 NOISE ANALYSIS

Connect to either cramer-rao or FX solutions in some way

Assume we did form visibilities with some integration time. Assuming the noise on each visibility, σ_{ab}, is independent, we can write the likelihood function of measuring V_{ab} given the true value, the gains, and the noise.

$$\mathcal{L}(V_{ab};\mathbf{g}) = \frac{1}{2\pi\sigma_{ab}^2} \exp\left[-\frac{\left|V_{ab} - g_a g_b^* V_{ab}^T\right|^2}{2\sigma_{ab}^2} \right] \tag{12}$$

Then the likelihood of the set of all visibilities will be,

$$\mathcal{L}(\mathbf{V};\mathbf{g}) = \prod_a \prod_{b>a} \mathcal{L}(V_{ab};\mathbf{g}) \tag{13}$$

The Fischer information matrix for the set of gain parameters is

$$\mathbf{F}_{ij}^g = \left\langle \frac{\partial \ln \mathcal{L}(\mathbf{V};\mathbf{g})}{\partial g_i} \frac{\partial \ln \mathcal{L}(\mathbf{V};\mathbf{g})}{\partial g_j} \bigg|_{\mathbf{g}} \right\rangle. \tag{14}$$

We next evaluate the derivate of the log-likelihood.

$$\frac{\partial \ln \mathcal{L}(\mathbf{V};\mathbf{g})}{\partial g_i} = \sum_{a\neq i} \frac{g_a^* V_{ai}^{T*} (V_{ai} - g_a g_i^* V_{ai}^T)}{2\sigma_{ai}^2} \tag{15}$$

This part of the argument needs serious work! In order to find the Cramér-Rao lower bound on the variance of the complex parameter, g_i, we consider the term of the Fischer matrix where the first derivative is taken with respect to g_i, and the second with g_i^*. The result is

$$\begin{aligned}\mathbf{F}^g_{ii} &= \left\langle \left[\sum_{a\neq i} \frac{g_a^* V_{ai}^{T*}(V_{ai} - g_a g_i^* V_{ai}^T)}{2\sigma_{ai}^2}\right] \times \right. \\ &\quad \left. \left[\sum_{b\neq i} \frac{g_b V_{bi}^T (V_{bi}^* - g_b^* g_i V_{bi}^{T*})}{2\sigma_{bi}^2}\right]\right\rangle \\ &= \sum_{a\neq i}\sum_{b\neq i} \frac{g_a^* g_b V_{ai}^{T*} V_{bi}^T}{4\sigma_{ai}^2\sigma_{bi}^2} \left\langle V_{ai}V_{bi}^* - g_i g_b^* V_{ai} V_{bi}^{T*} \right. \\ &\quad \left. - g_a g_i^* V_{ai}^T V_{bi}^* + g_a g_b^* |g_i|^2 V_{ai}^T V_{bi}^{T*}\right\rangle \end{aligned} \tag{16}$$

The expected values are easy to evaluate. Each visibility will average to the "true" value times the respective gains. The term with two visibilities will include a noise term.

$$\left\langle V_{ai} V_{bi}^*\right\rangle = |g_i|^2 g_a g_b^* V_{ai}^T V_{bi}^{T*} + \sigma_{ai}^2 \delta_{ab} \tag{17}$$

Here δ_{ab} is the Kronecker delta selecting the term where $a = b$ and the noise correlates. Plugging in the expectation values, equation 16 simplifies greatly to

$$\mathbf{F}^g_{ii} = \sum_{a\neq i} \frac{\left|g_a V_{ia}^T\right|^2}{4\sigma_{ai}^2} \tag{18}$$

Finally we relate our result to the theoretical best uncertainty we can place on our unknown gain parameter using the Cramér-Rao lower bound.

$$\sigma_{g_i}^2 \geq \left[\mathbf{F}^g_{ii}\right]^{-1} = \left[\sum_{a\neq i} \frac{\left|g_a V_{ia}^T\right|^2}{4\sigma_{ai}^2}\right]^{-1} \tag{19}$$

6 DISCUSSION

ACKNOWLEDGEMENTS

This work has been supported by the National Science Foundation through award AST-1206552.

REFERENCES

Bandura K., et al., 2014, in Society of Photo-Optical Instrumentation Engineers (SPIE) Conference Series. p. 22 (arXiv:1406.2288), doi:10.1117/12.2054950

Beardsley A. P., et al., 2012, MNRAS, 425, 1781

Bhatnagar, S. Cornwell, T. J. Golap, K. Uson, J. M. 2008, A&A, 487, 419

Bowman J. D., et al., 2013, Publ. Astron. Soc. Australia, 30, 31

Bunton J. D., 2004, Experimental Astronomy, 17, 251

Cohen A. S., Lane W. M., Cotton W. D., Kassim N. E., Lazio T. J. W., Perley R. A., Condon J. J., Erickson W. C., 2007, AJ, 134, 1245

Daishido T., et al., 2000, Proc. SPIE, 4015, 73

Ellingson S. W., et al., 2013, IEEE Transactions on Antennas and Propagation, 61, 2540

Foster G., Hickish J., Magro A., Price D., Zarb Adami K., 2014, Monthly Notices of the Royal Astronomical Society, 439, 3180

Kassim N. E., et al., 2007, ApJS, 172, 686

Lonsdale C. J., Doeleman S. S., Cappallo R. J., Hewitt J. N., Whitney A. R., 2000, in Butcher H. R., ed., Society of Photo-Optical Instrumentation Engineers (SPIE) Conference Series Vol. 4015, Radio Telescopes. pp 126–134

Mellema G., et al., 2013, Experimental Astronomy, 36, 235

Mitchell D., Greenhill L., Wayth R., Sault R., Lonsdale C., Cappallo R., Morales M., Ord S., 2008, Selected Topics in Signal Processing, IEEE Journal of, 2, 707

Morales M. F., 2011, PASP, 123, 1265

Morales M. F., Matejek M., 2009, MNRAS, 400, 1814

Otobe E., et al., 1994, PASJ, 46, 503

Parsons A. R., et al., 2010, The Astronomical Journal, 139, 1468

Tegmark M., 1997, ApJ, 480, L87

Tegmark M., Zaldarriaga M., 2009, Phys. Rev. D, 79, 083530

Tegmark M., Zaldarriaga M., 2010, Phys. Rev. D, 82, 103501

Thornton D., et al., 2013, Science, 341, 53

Thyagarajan N., Beardsley A. P., Bowman J. D., Morales M. F., 2015, arXiv:1510.08318

Tingay S. J., et al., 2013, PASA - Publications of the Astronomical Society of Australia, 30

Wijnholds S., van der Veen A.-J., 2009, Signal Processing, IEEE Transactions on, 57, 3512

Zheng H., et al., 2014, MNRAS, 445, 1084

de Vos M., Gunst A., Nijboer R., 2009, Proceedings of the IEEE, 97, 1431

van Haarlem M. P., et al., 2013, A&A, 556, A2

APPENDIX A: SOME EXTRA MATERIAL

If you want to present additional material which would interrupt the flow of the main paper, it can be placed in an Appendix which appears after the list of references.

This paper has been typeset from a TEX/LATEX file prepared by the author.